Central European Journal of Energetic Materials
ISSN 1733-7178; e-ISSN 2353-1843

Cent. Eur. J. Energ. Mater. 2023, *20*(3): 340-363; DOI 10.22211/cejem/173058
Article is available in PDF-format, in colour, at:
https://ipo.lukasiewicz.gov.pl/wydawnictwa/cejem-woluminy/vol-20-nr-3/

Research paper

The Flow and Heat Transfer Behaviour of Liquid COMP-B3 in Slow Cook-off

Jie Zhou[1)], **Shuai Wang**[2)], **Zide Liu**[3)], **Haiyan Zhang**[4)], **Aiguo Pi**[1,*)]

[1)] *State Key Laboratory of Explosion Science and Technology, Beijing Institute of Technology, Beijing, 100000, PR China.*

[2)] *Hubei Institute of Aerospace Chemical Technology, Xiangyang, 441000, PR China.*

[3)] *Science and Technology on Transient Impact Laboratory, No.208 Institute of China Ordnance Industries, Beijing, 102200, PR China.*

[4)] *Mechanical and Electrical College, North University of China, Taiyuan, 030051, PR China.*

* *E-mail:* aiguo_pi@bit.edu.cn

Abstract: In order to investigate the flow and heat transfer characteristics of COMP-B3 under thermal stimulation, a series of slow cook-off experiments were designed and conducted, encompassing different sample sizes and heating conditions. The internal temperature profiles were captured using a high-speed data acquisition system. Subsequently, the internal flow and heat transfer conditions of the liquid COMP-B3 were analyzed through numerical simulations employing a non-Newtonian flow model. The results demonstrated the presence of heat convection within the liquid COMP-B3, regardless of sample sizes or heating conditions. However, it should be noted that the occurrence of heat convection is not necessarily observed at the onset of melting. The overall cook-off process can be categorized into three phases: solid (with melting), thermal conduction, and thermal convection. If convection occurs prior to the self-heating reaction, the direction of the flow field within the liquid COMP-B3 experiences a reversal near ignition. Additionally, a predictive method for the flow behaviour inside the

liquid COMP-B3 during slow cook-off is proposed. Rough estimates of the flow conditions can be made based on the charge temperature, the internal temperature difference, and the characteristic length. Importantly, these phenomena are theoretically applicable to a wide range of mixed melt-cast explosives, extending beyond COMP-B3. The results provide additional reference value for further investigations into the ignition characteristics of mixed melt-cast explosives under thermal stimulation.

Keywords: COMP-B3, Slow Cook-off, Bingham fluid, viscose flow, heat convection

1 Introduction

Energetic materials play a crucial role in various applications, including munitions, mining, and construction. Among these materials, Composition B (COMP-B) is a well-known mixed melt-cast explosive composed of 2,4,6-trinitrotoluene (TNT) and hexahydro-1,3,5-trinitro-1,3,5-triazine (RDX) [1]. The specific composition of COMP-B can vary, but it typically consists of a blend of these two primary ingredients. Notably, when the mass ratio of RDX to TNT is 40:60, it is referred to as COMP-B3.

Unlike RDX, TNT transitions into a liquid state when the ambient temperature surpasses its melting point. However, the RDX particles remain as a suspended solid. The suspension exhibits complex flow characteristics, which result in COMP-B displaying characteristics different from solid or pure melt-cast explosives in slow cook-off tests.

In Wardell's Scaled Thermal Explosion Experiment (STEX) tests, the ignition location differed for COMP-B and PBX-9501. For COMP-B, the highest temperature was observed in the upper part of the explosive when it ignited, whereas for PBX-9501, it was in the middle part. This discrepancy can be attributed to the presence of thermally-driven convective heat transfer in the molten COMP-B, which influences the location of the self-heating area [2]. McClelland's subsequent tests [3, 4] verified this phenomenon. By incorporating the buoyancy of the different species in the system (solid and liquid) into the simulation model, the numerical simulations showed that convection was present in the heating process, which in turn caused a change in the temperature distribution. However, it is important to note that in McClelland's tests, the temperature distribution within COMP-B changed only when the internal temperature reached approximately 428 K, rather than at the beginning of COMP-B melting. This indicates that the molten COMP-B became flowable only

when the internal temperature exceeded 428 K, which differs significantly from McClelland's simulation results. Additional experimental evidence supporting the existence of convection in molten COMP-B was presented by Glascoe [5]. Using a high-speed photographic apparatus in the STEX tests, it was observed that COMP-B ignited at the upper part of the vessel in slow cook-off tests. While the above studies confirm the existence of convection in molten COMP-B, the flow behaviour of the liquid charges throughout the entire cook-off process remains unclear.

Asante *et al.* [6] and McCallen *et al.* [7] both concluded that molten TNT ignited at the upper part of the vessel in cook-off tests of pure TNT. In a comparative analysis of flow behaviour and temperature evolution between COMP-B and TNT, Hobbs *et al.* [8, 9] discovered that a molten COMP-B suspension exhibited solid-like behaviour even after complete melting, which was different from the molten TNT in their tests. Subsequently, when the internal temperature reached approximately 413 K in the experiment, the viscosity of molten COMP-B suddenly decreased. Based on the fitting results obtained from numerical simulations, Hobbs *et al.* [8, 9] believed that the viscosity of molten COMP-B experienced a significant decrease from $2.5 \cdot 10^5$ to 0.2 Pa·s in a very short time at that temperature. They further noted that the viscosity of the TNT/RDX suspension cannot be regarded as a constant or described with a simple expression of temperature. It is suspected that the abrupt drop in the suspension's viscosity was strongly related to the RDX particles.

It is evident that a molten COMP-B suspension is not a Newtonian fluid [10]. The viscosity of COMP-B3 at elevated temperatures was investigated by Zerkle using a falling ball viscometer [11]. In that work, a viscosity model that included the temperature, strain rate, and particle volume fraction was presented. Subsequently, Hobbs *et al.* [12] incorporated this viscosity model into the slow cook-off simulation of COMP-B3. However, they found that Zerkle's model was too flowable and that the simulation results did not match well with the cook-off tests. Davis *et al.* [13-15], in subsequent research, found the rheological behaviour of molten COMP-B3 and TNT/HMX suspensions fitted in well with those of Bingham plastics. Davis *et al* introduced a yield criterion to Zerkle's model and proposed a viscosity model for molten COMP-B3 based on Bingham fluid behaviour. They used the model to simulate the motion of a falling ball in molten COMP-B3, and it fitted well with the tests.

In summary, although the sudden drop in viscosity of liquid COMP-B3 has been observed in various studies, its detailed flow behaviour remains unclear. In the present study, a series of cook-off tests for COMP-B3 with different sample sizes and heating rates, was conducted. The temperature variations within the

charge were recorded using embedded temperature sensors and a high-speed data acquisition system. By incorporating Davis's viscosity model into the cook-off simulations of COMP-B3, the flow and heat transfer characteristics of the liquid charge were further investigated. As a result, an explanation for the presence of heat convections within liquid COMP-B3 during the slow cook-off process is presented. Additionally, a method for predicting the flow behaviour inside the liquid COMP-B3 was established.

2 Experimental Method

2.1 Test design

The cook-off system used in this study comprised several key components, including a temperature controller (Shimaden MR-13, Japan), a temperature data logger (Fluke 1586A, USA), a disposable heating box, and a test sample, as illustrated in Figure 1(a). The heating box, shown in Figures 1(b) to 1(c), had a maximum power capacity of 3 kW and consisted of a barrel, a scaffold, multiple electric heating stripes, and insulation made of rock wool. The test sample was vertically centered in the barrel by using a metallic frame.

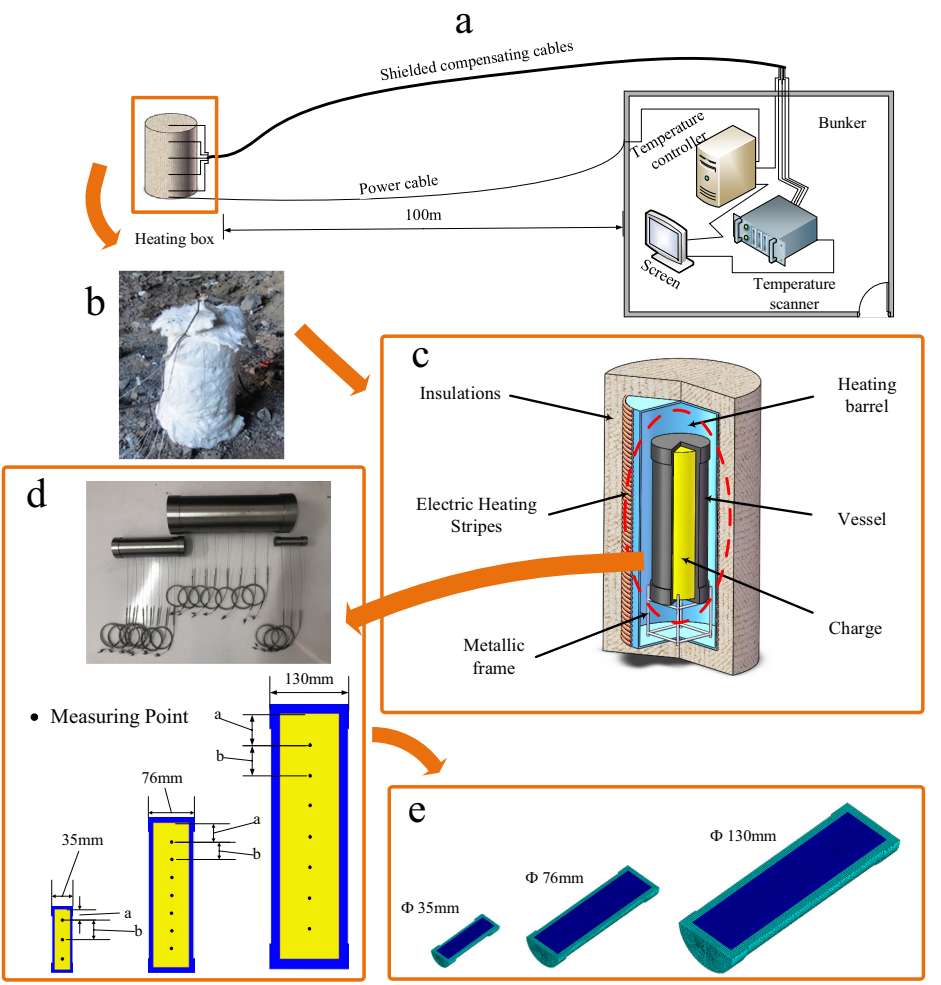

Figure 1. Test design and description

2.2 Test samples

Three types of C45E4 steel containers were used, where COMP-B3 was charged. Each charge had a length to diameter ratio of approximately 4:1, as depicted in Figure 1(d). The specific details of each test sample can be found in Table 1.

Table 1. Details of each test sample

Diameter of vessel [mm]	Length of vessel [mm]	Wall thickness [mm]	Diameter of charge [mm]	Length of charge [mm]	Space [mm]	
					a	b
35	112	3.5	28	105	17.5	35
76	255	7.5	61	240	30	
130	430	15	100	400	50	

Evenly spaced pinholes, 0.9 mm diameter, were drilled along the axis on the side face of each vessel. During the casting process of the explosive, temperature sensors were embedded through the pinholes and positioned at the center of each charge. After cooling, the pinholes were sealed with silicone rubber to ensure airtightness and prevent leakage.

In order to minimize the interference of the temperature sensors on the flow of liquid COMP-B3 during and after melting, 0.8 mm diameter K-type sheathed thermocouples were used. The thermocouple probe was designed to be thin to minimize disruption to the flow characteristics. The measuring points inside the charge were marked 1~3 or 1~7, indicating the sequential numbering from the top to the bottom of the charge. This allowed for temperature measurements at different depths within the charge in order to observe the temperature distribution and changes during the slow cook-off process.

2.3 Heating method

The heating box's effective power output was dynamically regulated by the MR-13 temperature controller. This controller utilized a PID (proportion-integration-derivation) algorithm to continuously compare the actual temperature measured on the outer surface of the vessel with the set value. The controller made adjustments to the output power every second to achieve precise temperature control. By appropriately tuning the control parameters, the temperature of the vessel could be precisely regulated according to a predefined heating rate. This control mechanism ensured precise and consistent heating conditions for the slow cook-off experiments.

The heating rates employed in this study were determined based on the guidelines outlined in the standardization agreement of NATO (North Atlantic

Treaty Organization) for slow cook-off test procedures (STANAG 4382) and other relevant research papers [16-21]. Two different heating rates were selected to represent both faster (1 K/min) and slower (3.3 K/h) heating conditions.

For the slower heating condition, the temperature of the vessel was initially raised at a rate of 10 K/h until it reached 323 K. It was then maintained at 323 K for approximately 1 h. After this holding period, the temperature was further increased at the rate of 3.3 K/h until the charge experienced ignition or combustion.

A total of six experiments were conducted in this study, labelled as S-1, S-3.3, M-1, M-3.3, L-1, and L-3.3. The leading letters in each label denote the size of the vessel used in the experiment, while the numbers indicated the corresponding heating rates. Specifically:

– "S" referred to the small-sized vessel,
– "M" referred to the medium-sized vessel,
– "L" referred to the large-sized vessel,
– "1" indicated the faster heating rate of 1 K/min,
– "3.3" indicated the slower heating rate of 3.3 K/h.

These labels were assigned to distinguish between the different combinations of vessel sizes and heating rates employed in the experiments, enabling clear identification and categorization of the test conditions.

3 Numerical Simulation

3.1 Assumptions

In the numerical simulations for the cook-off process, several simplifying assumptions were made to streamline the calculation model. These assumptions include:

(i) Heat convection and heat conduction were considered as the primary heat transfer mechanisms during the cook-off process, while radiation was neglected.

(ii) The liquid COMP-B was treated as an incompressible fluid, and its density was solely dependent on temperature. The impact of pressure was not taken into account.

(iii) The decomposition of COMP-B3 was assumed to follow a one-step, two-species reaction, with only temperature influencing the reaction rate.

To facilitate the simulation, 3D grid models of each test sample were generated and meshed using the ANSYS ICEM CFD software [22], as shown in Figure 1 (step (e)).

3.2 Reaction model

Based on the Frank-Kamenetskii reaction model and the Arrhenius equation, the heat generated by the thermal decomposition reaction of the explosive (Q_m) can be expressed using Equation 1 [23]:

$$Q_m = \rho_c Q A e^{-\frac{E_a}{RT}} \tag{1}$$

where ρ_c is the density of the explosive, which will be discussed later. Q represents the reaction heat of the explosive per unit mass. A is a pre-exponential factor, and E_a and R refer to the activation energy and the universal gas constant, respectively. The values for E_a and R can be found in Table 2.

Table 2. Reaction model parameters [24]

Symbol	Description	Unit	Value
E_a	Activation energy	J/mol	22000
Q	Reaction enthalpy	J/kg	$5.86 \cdot 10^6$
A	Pre-exponential factor	1/s	$e^{35.67}$
R	Universal gas constant	J/(mol·K)	8.31451

3.3 Viscosity model

COMP-B3, which consists of TNT and RDX, exhibits non-Newtonian behaviour when completely molten. TNT, being one of the components, transitions into a liquid phase when the ambient temperature exceeds its melting point. On the other hand, RDX remains in the solid state, creating a suspension in the molten TNT. While molten TNT is known to exhibit typical Newtonian fluid behaviour [25-28], when a Newtonian fluid is filled with a high load of solid particles, the presence of these particles alters its flow characteristics. In such cases, the suspension does not follow Newtonian fluid behaviour and is commonly referred to as a Bingham plastic [29, 30]. The rheological characteristics of this suspension play a significant role in determining the overall flow and heat transfer characteristics of COMP-B3 during the slow cook-off process.

In this study, a viscosity model based on the Bingham fluid behaviour, as proposed by Zerkle *et al.* [11] and Davis *et al.* [13-15], was employed to characterize the fluidity of liquid COMP-B3 during the slow cook-off process. The viscosity model can be expressed using the following equations:

$$\mu = \alpha\left(T - T_m\right)^{\beta}\left(1 - \frac{\varphi}{\varphi_{\max}}\right)^{-2} + W\left(\varphi - \varphi_c\right)^{m} \cdot \frac{1 - \exp(-\left(B\left(\varphi - \varphi_c\right)^{n} + c\right) \cdot \gamma)}{\gamma} \tag{2}$$

$$\varphi_{\max} = \left(\frac{1}{\varphi_1} - \left(\frac{1}{\varphi_1} - \frac{1}{\varphi_\infty} \right) \left(\frac{1}{1 + D\gamma^P} \right) \right)^{-1} \tag{3}$$

$$\varphi = (0.6 - a_0 + a_1 T' + a_2 T'^2 + a_3 T'^3) \frac{\rho_C}{\rho_R} \tag{4}$$

$$T' = \frac{T - T_{m.TNT}}{T_{m.RDX} - T_{m.TNT}} \tag{5}$$

This model accounts for the flow characteristics of the suspension, considering both the presence of the molten TNT and the solid RDX particles, and provides a basis for simulating the motion and flow of liquid COMP-B3 during the slow cook-off process. In the viscosity model for liquid COMP-B3, the viscosity (μ) is influenced by various factors, including the local temperature (T), the particle volume fraction of solid RDX (φ), the maximum particle volume fraction of solid RDX that can be supported in the liquid COMP-B3 ($\varphi_{\max}$), and the strain rate (γ). The model incorporates additional parameters, which are outlined in Table 3, along with their corresponding values. The thermo-physical parameters of COMP-B3 and the C45E4 steel that were used in the heat transfer calculations are summarized in Tables 4 and 5.

Table 3. Viscosity model parameters

Symbol	Description	Unit	Value	Ref.
T_m	Melting point of COMP-B3	K	353	[11]
φ_C	Critical particle volume fraction of RDX	–	0.336	[14]
φ_∞	Limiting volume fraction of RDX in high strain	–	0.713	[11]
φ_1	Limiting volume fraction of RDX in low strain	–	0.55	[31]
ρ_R	Density of RDX	kg/m^3	1820	[32]
ρ_C	Density of COMP-B3	kg/m^3	for $T \leq T_s$: 1690 for $T > T_s$: $1690 - 0.675(T - T_s)$	[4]
T_s	Solid temperature of COMP-B3	K	353.15	[24]

Table 3. continuation

Symbol	Description	Unit	Value	Ref.
α	Fitted parameter	–	0.0127	[11]
β		–	0.304	[11]
W		–	6874	[14]
m		–	2.37	[14]
B		–	$1.76 \cdot 10^6$	[13]
n		–	4	[13]
c		–	100	[13]
D		–	8.73	[31]
P		–	–0.398	[31]
a_0		–	0.0426	[4]
a_1		–	0.0753	[4]
a_2		–	0.1340	[4]
a_3		–	0.7474	[4]
$T_{m.TNT}$	Melting point of TNT	K	354.15	[4]
$T_{m.RDX}$	Melting point of RDX	K	478.15	[4]

Table 4. Thermo-physical parameters of COMP-B3 [24]

Parameter	Unit	Value
Thermal conductivity	W/(m·K)	for $T < T_s$: 0.17 for $T_s \leq T \leq T_1$: $0.17 - 0.025(T - T_m)$ for $T > T_1$: 0.15
Specific heat	J/kg	$2.1538T + 413.15$
Melting enthalpy	J/kg	128000

Table 5. Thermo-physical parameters of C45E4 steel [33]

Parameter	Unit	Value
Density	kg/m^3	7850
Specific heat	J/kg	475
Thermal conductivity	W/(m·K)	44

The viscosity model, boundary conditions, and reaction model were implemented in the FLUENT software using user-defined function (UDF). The heating rates were specified as 1 K/min and 3.3 K/h. All initial conditions were set according to the actual experimental tests.

4 Results

The measured ignition temperatures for each test are shown in Figure 2. In the M-1 and M-3.3 tests, two thermocouples were damaged during the experiments for unknown reasons, resulting in missing temperature data for those specific points. However, despite this setback, it does not hinder the analysis of the test data as a whole. The remaining temperature data from the other sensors can still provide valuable insights and enable a comprehensive analysis of the ignition behaviour.

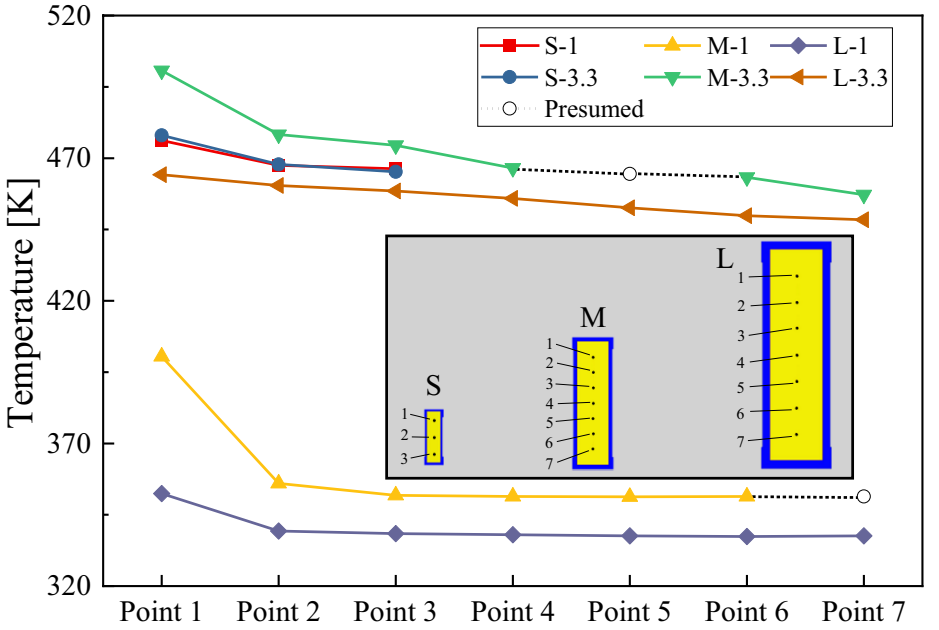

Figure 2. Temperatures inside the vessels when ignition occurred

Figure 3 displays a comparison between the measured (left-hand side plots) and the simulation temperatures (right-hand side plots), along with the calculated average flow velocity curves. Additionally, temperature contours are provided at several specific points within the simulation.

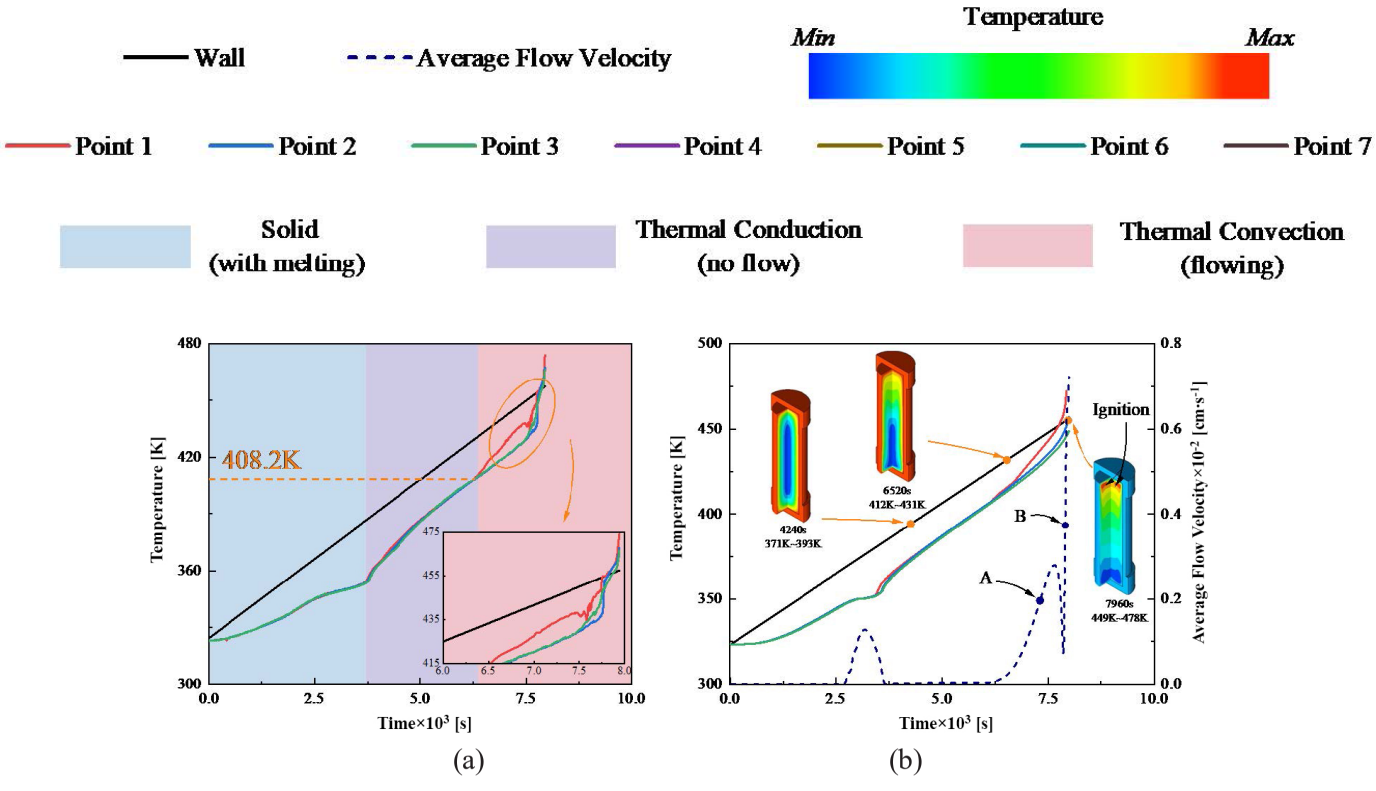

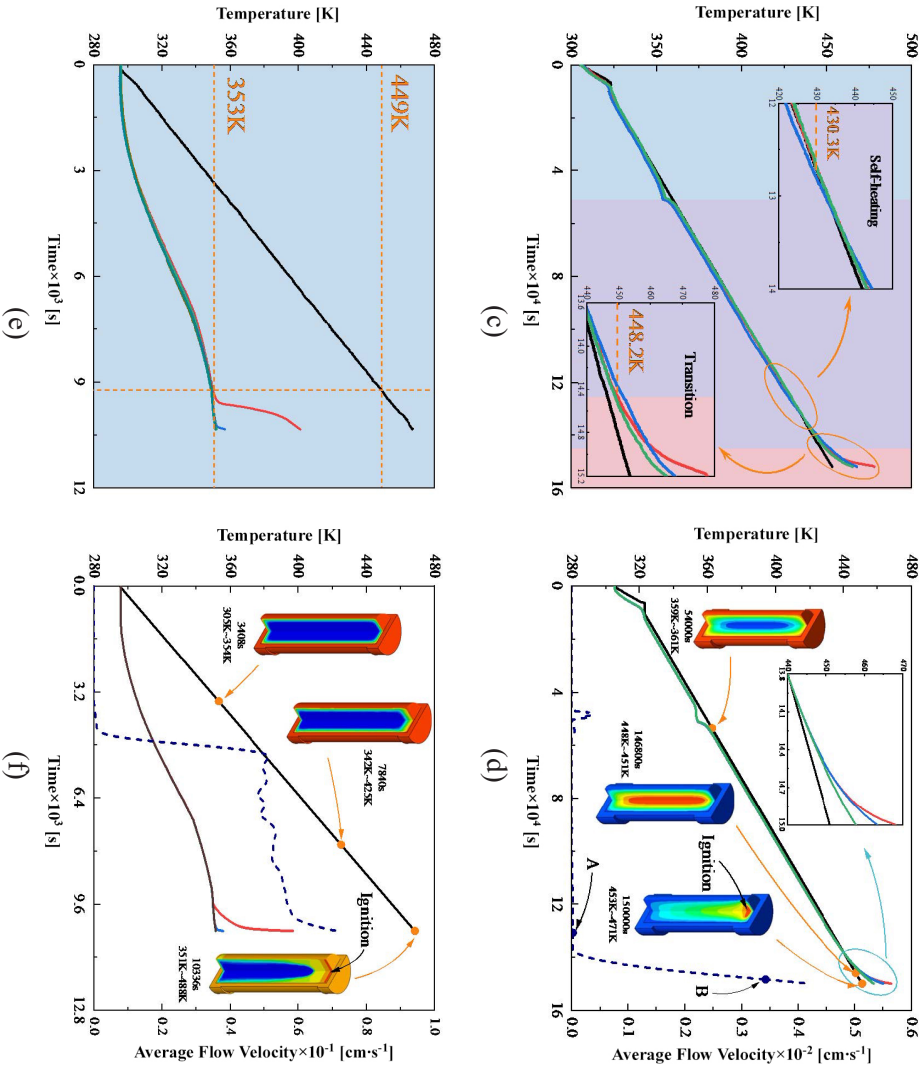

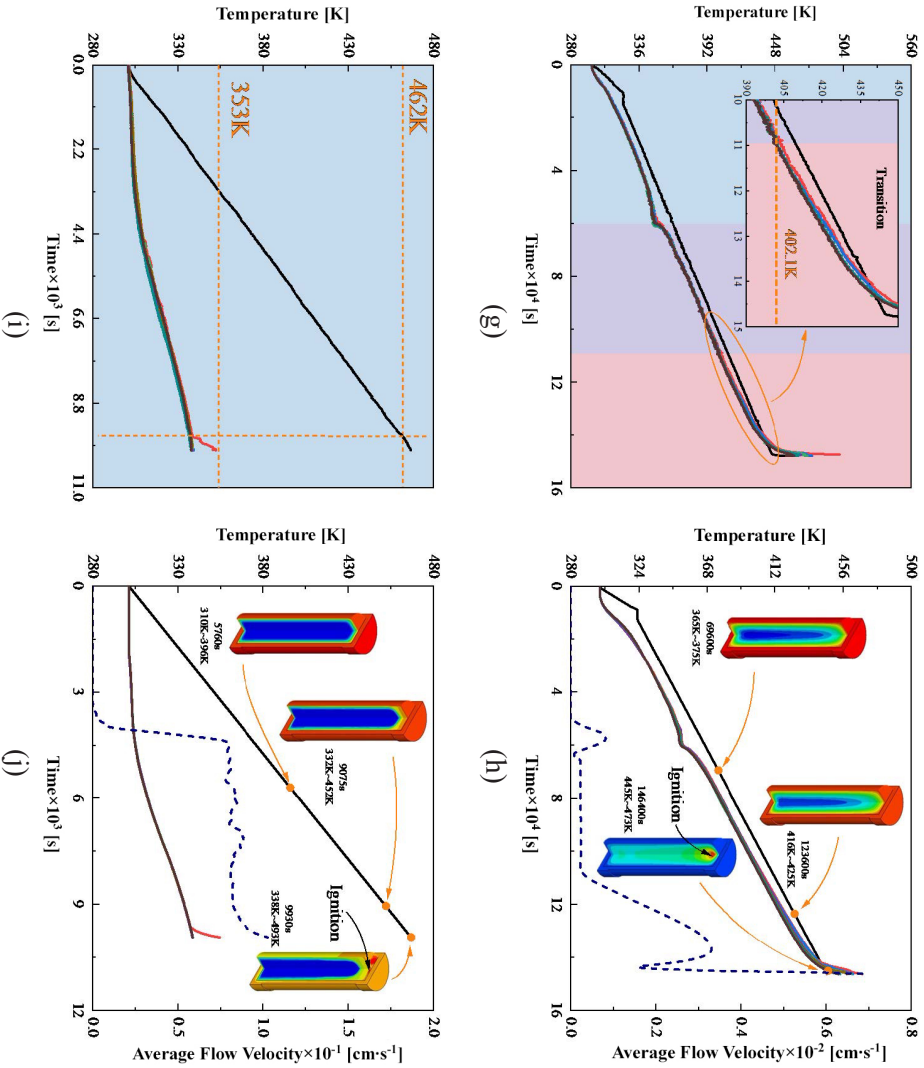

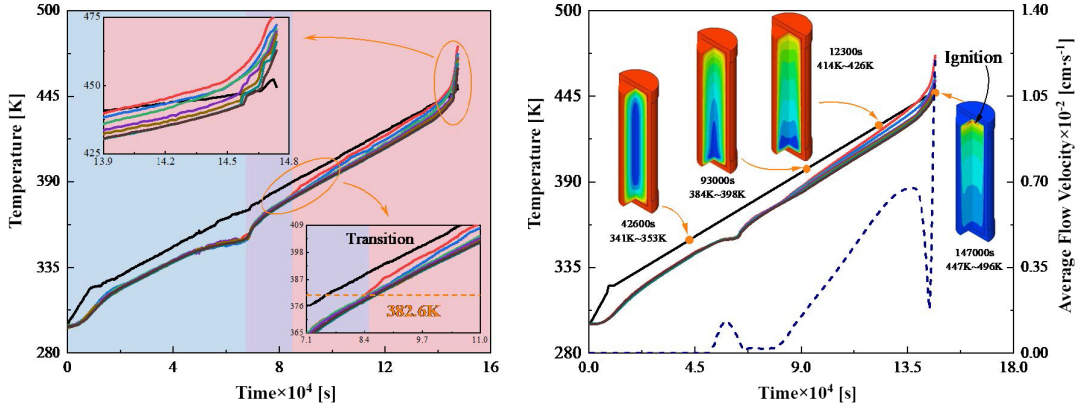

(k) (l)

Figure 3. A comparison between the measured (left-hand side plots) and the simulation temperatures (right-hand side plots):
– experiments for S-1 (a), S-3.3 (c), M-1 (e), M-3.3 (g), L-1 (i) and L-3.3 (k),
– simulations for S-1 (b), S-3.3 (d), M-1 (f), M-3.3(h), L-1(j) and L-3.3 (l)

5 Discussion

5.1 Temperature

As depicted in Figure 2, the larger the volume of the sample or the faster the rate of temperature increase, the greater the temperature differences within the sample. Additionally, the results of each test indicated that the temperature at point 1 (top of the explosive) reached the highest value upon ignition. Moreover, the measured results consistently demonstrate a progressive decrease in temperature from top to bottom inside the vessel when ignition occurred. This observation suggests that ignition occurred in the top area of the vessel across all test types. The temperature contours in the simulations, as depicted in Figure 3 (shown in the right-hand side plots), further confirm this inference.

As illustrated in Figure 3(a), during the S-1 test, it was hard to differentiate the temperatures of individual measuring points after the COMP-B3 melted. However, as the internal temperature approached approximately 408 K, the temperature at point 1 exhibited increasingly higher temperatures compared to the other points. Eventually, the test sample ignited when the wall temperature reached approximately 457 K. Notably, when that occurred, the distribution of internal temperatures appeared to follow a certain order. The temperature in the top portion was higher than the temperature in the bottom portion of the vessel at a given time, as depicted in Figure 3(b).

In the case of the slower heating condition (S-3.3), depicted in Figure 3(c), the behaviour was distinct. After the complete melting of the charge, the internal temperature distribution remained relatively unchanged for an extended period, resembling the pre-melting state. It was only when the temperature inside the charge reached approximately 430 K that the self-heating reaction commenced, leading to the release of energy. Consequently, the temperature inside the charge increased more rapidly than the temperature at the vessel's surface. In Figure 3(d), it can be observed that when ignition occurred, the hottest area of the explosive was near point 1. However, the self-heating reaction first manifested itself at the center of the vessel.

As depicted in Figures 3(e) and 3(i), the temperature profiles of the M-1 and L-1 tests exhibited similarities. At the onset of the tests, there was a rapid increase in the temperature difference between the center and the surface of the charge in both cases. As the explosives next to the inner surface of the vessel began melting, a significant amount of heat was absorbed, causing a deceleration in the temperature rise within the charge. Furthermore, point 1 displayed the highest temperature when ignition occurred, while most of the other measuring points remained below the melting point of the explosive. This suggests that

the majority of the explosive remained in a solid state during the M-1 and L-1 tests. Moreover, it was observed that the upper part of the charge melted faster than the lower part; this is supported by the temperature contours presented in Figures 3(f) and 3(j).

For the slow heating rate, the temperature traces of M-3.3 and L-3.3 (Figures 3(g) and 3(k)) appear to be similar to the temperature traces of S-1 (Figure 3(a)), despite having a different chamber size and different heating rates. After the explosives had melted completely, the internal temperature distribution remained similar to the pre-melting stage. It was not until the inside charge reached about 402 K for M-1 or 382 K for L-1 that the upper part started to become hotter than the lower part until ignition. Eventually, the temperature at point 1 became the highest. In the L-3.3 test, the temperature stratification was more pronounced due to a greater difference in internal temperatures, as shown in Figures 3(h) and 3(l).

5.2 Flow and convection

The average flow velocity within the molten charge, as illustrated in Figures 3(b), 3(d), 3(h) and 3(l), was directly obtained from the simulation results in the FLUENT software. Interestingly, the results indicated that even when the charges were completely melted, the average velocity of the flow field remained very low. This suggests that heat conduction was the main mode of heat transfer inside the explosive at that time, and that the suspensions were nearly stationary. The influence of heat convection on the internal temperature distribution was minimal. As the temperature increased, the viscosity of the charge (now liquid) decreased until it reached a point where it yielded and started to flow. Under the influence of gravity and buoyancy, convection occurred, resulting in an increase in the intensity of the flow field.

In the case of S-3.3, the average flow velocity inside the liquid explosive continued to increase until ignition, as depicted in Figure 3(d). However, in the cases of S-1, M-3.3, and L-3.3, as shown in Figures 3(b), 3(h) and 3(l), the flow velocity initially increased after the suspension yielded, but then experienced a significant drop before rising again near ignition. This phenomenon can be attributed to the flow behaviour and the occurrence of the self-heating reaction.

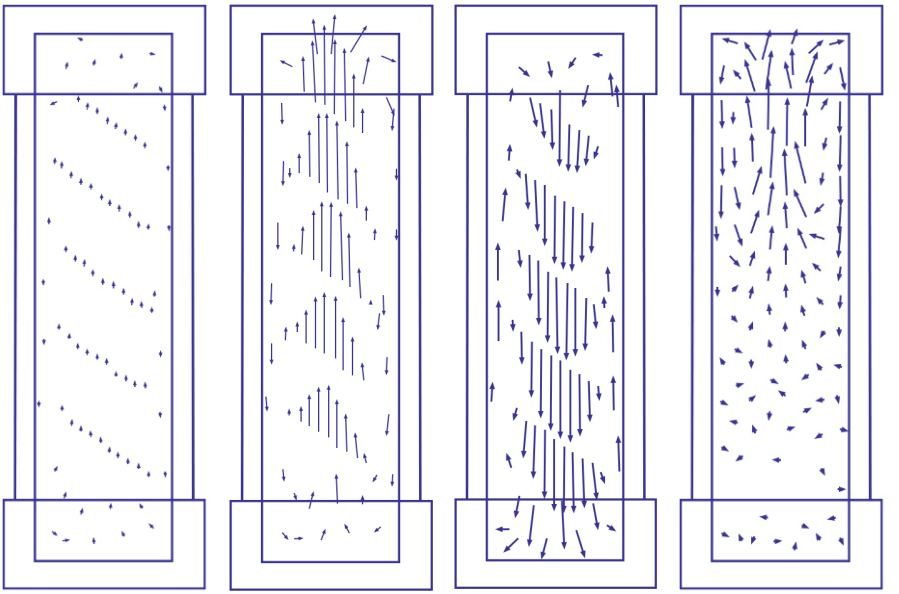

(a) (b) (c) (d)

Figure 4. Flow traces of S-3.3 before self-heating (a), S-3.3 after self-heating (b), S-1 before self-heating (c) and S-1 after self-heating (d)

In the case of S-3.3, prior to the occurrence of the self-heating reaction, the temperature difference between the surface of the vessel and the inside of the charge was negligible. The flow field intensity remained relatively low for a significant period after the charge had melted. The flow traces of point A in Figure 3(d) are depicted in Figure 4(a). Subsequently, as the self-heating reaction initiated at the center, heat started to accumulate in the central region of the charge, leading to an increase in the temperature difference within the liquid explosive. Eventually, buoyancy forces drove the hot liquid to flow and rise to the top of the vessel near ignition. The flow traces of point B in Figure 3(d) are shown in Figure 4(b).

However, the simulation of S-1 showed a significant difference. The average flow velocity in S-1 exhibited a significant drop followed by an increase when it approached ignition. We believe that this behaviour is likely due to the redirection of the flow field inside the vessel. Prior to the onset of the self-heating reaction, the liquid charge had undergone yielding, resulting in the appearance of buoyancy-driven flow. The fraction of liquid charge at the vessel surface was hotter than that at the center, causing the hotter liquid with lower density to flow along the internal surface towards the top of the vessel. Subsequently,

it cooled down and flowed along the center towards the bottom, leading to the accumulation of the hot fraction at the top. The flow traces of point A in Figure 3(b) are shown in Figure 4(c). Once the self-heating reaction initiated at the top of the charge, where this region became hotter than the surface, the direction of flow circulation was completely reversed. The flow traces of point B in Figure 3(b) are shown in Figure 4(d). Initiated by the self-heating reaction, following the yielded flow, the redirection of the flow field resulted in a sharp decrease and subsequent increase in the average flow velocity near ignition.

5.3 Estimation of yield flowing

Based on the physical and flow characteristics of the charge, the entire cook-off process can be divided into three stages, as illustrated in Figure 3. The first stage is the solid phase with melting (light blue), which occurs from the beginning until the complete melting of the charge. The second stage is thermal conduction (lavender). During this period, when the charge is fully liquid, but due to its high viscosity, the non-uniform temperature suspension remains stationary, and no convection occurs. The final stage is thermal convection (light pink), which begins with the flow of the liquid charge and continues until ignition. As the temperature increases, more RDX dissolves, resulting in a decrease in the viscosity of the liquid charge. This decrease in viscosity, along with the temperature differences caused by the self-heating reaction, overcomes the resistance. Consequently, the liquid charge starts to flow, and convection changes the temperature distribution inside the vessel.

Except for M-1 and L-1, the transition from thermal conduction to thermal convection was observed in all of the other four tests, albeit at different temperatures. This transition can be described by the Rayleigh number (*Ra*), which characterizes the behaviour of fluids when there are non-uniformities in mass density, typically caused by temperature differences [34].

$$Ra = \frac{\Delta\rho g L^3}{\mu\alpha} = \frac{\rho\beta\Delta T g L^3}{\mu\alpha} \tag{6}$$

where ρ is the fluid density, β is the thermal expansion coefficient, ΔT is the temperature difference, g is the gravitational acceleration, L is the characteristic length, μ is the viscosity, and α is the thermal diffusivity. When the Rayleigh number Ra is below a critical value, there is no flow, and heat transfer occurs mainly through conduction. However, when the Rayleigh number exceeds the critical threshold, heat is transferred through thermal convection.

For the yielded liquid charge, ρ and μ exhibited minimal changes with temperature, β, α and g were constant. Thus:

$$Ra \propto \Delta TL^3 \tag{7}$$

where the radius of each charge is denoted as L. T_0 represents the transition temperature, which is determined from the measured charge temperatures at the transition point indicated in Figure 3. This transition point is identified by a noticeable divergence in the measured temperatures of the liquid charge among the different measurement points. ΔT represents the temperature difference between the charge center and the surface. The temperature characteristics of each test at the transition from thermal conduction to thermal convection are shown in Table 6. Data from Table 6 were fitted with temperature in an exponential function, as shown in Figure 5.

Table 6. Temperature characteristics of transition

Label	T_0 [K]	ΔT [K]	L [mm]	ΔTL^3 [K·mm^3]
S-1	408.2	22.2	14	60917
S-3.3	446.5	2.1	14	5762
M-3.3	409.4	7.3	30.5	207120
L-3.3	382.6	7.7	50	962500
–	427.2*	4*	25.4*	65548*

* Taken from Ref. [4]

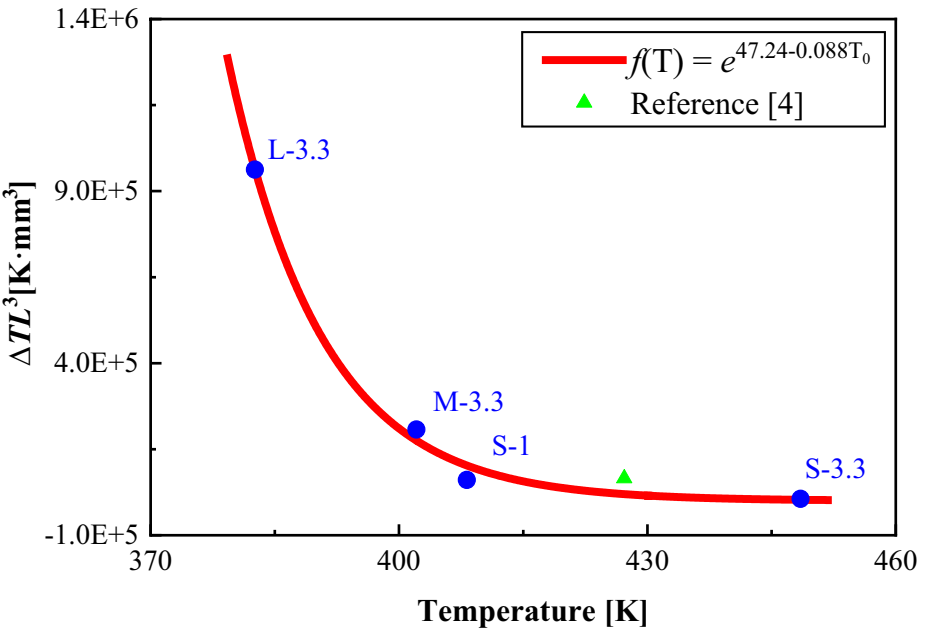

Figure 5. Fitted transition parameters

Hence a criterion can be proposed to roughly predict the flow inside the liquid charge in slow cook-off tests based on experimental results:

$$\lambda = \Delta T \cdot L^3 - \exp(47.24 - 0.088T) \tag{8}$$

where λ is used to determine whether flow occurs at a certain temperature. If $\lambda < 0$, the liquid charge can quite possibly remain stationary even it is fully melted, or, conversely, the thermal convection is possibly already happening in the suspension when $\lambda > 0$.

6 Conclusions

- In slow cook-off tests of COMP-B3 (RDX/TNT = 40:60), natural convection does exist, but it may not necessarily occur at the beginning of the explosive's melting. The entire cook-off process can be divided into three stages: solid (with phase change), thermal conduction, and thermal convection.
- After the complete melting of COMP-B3, if convection occurs before the self-heating reaction, the flow field direction near ignition will be reversed,

or conversely, it will remain uninterrupted. Due to the influence of thermal convection, COMP-B3 will ignite at the top side during slow cook-off.

- In the studies of the flow and heat transfer characteristics of COMP-B3 in the slow cook-off, all the affecting factors that have been discussed in the past studies, such as lengths, diameters, and heating rates, can be ultimately categorized as the impact of temperature differences on the flow behaviour.
- An estimation method for predicting the flow behaviour inside the liquid COMP-B3 during slow cook-off is proposed based on the calculation of the Rayleigh number. The flow conditions can be roughly predicted by considering the charge temperature, the inside temperature difference, and the characteristic length.

References

[1] Hobbs, M.L.; Kaneshige, M.J.; Erikson, W.W.; Brown, J.A.; Anderson, M.U.; Todd, S.N.; Moore, D.G. Cookoff Experiments of a Melt Cast Explosive (Comp-B3). *Combust. Flame*. **2020**, *213*: 268-78; https://doi.org/10.1016/j.combustflame.2019.12.004.

[2] Wardell, J.; Maienschein, J. The Scaled Thermal Explosion Experiment. *Proc. 12th Int. Detonation Symp.,* San Diego, US-CA, **2002**.

[3] McClelland, M.A.; Maienschein, J.L.; Reaugh, J.E.; Tran, T.D.; Nichols, A.L.; Wardell, J.F. ALE3D Model Predictions and Experimental Analysis of the Cookoff Response of Comp B. *JANNAF Meeting*, Colorado Springs, US, **2003**.

[4] McClelland, M.A.; Glascoe, E.A.; Nichols, A.L.; Schofield, S.P.; Springer, H.K. ALE3D Simulation of Incompressible Flow, Heat Transfer, and Chemical Decomposition of Comp B in Slow Cookoff Experiments. *Proc. 15th Int. Detonation Symp.,* San Francisco, US-CA **2014**.

[5] Glascoe, E.A.; Dehaven, M.R.; McClelland, M.; Greenwood, D.W.; Springer, H.K.; Maienschein, J.L. Mechanisms of Comp-B Thermal Explosions. *Proc. 15th Int. Detonation Symp.,* San Francisco, US-CA, **2014**.

[6] Asante, D.O.; Kim, S.; Chae, J.; Kim, H.; Oh, M. CFD Cook-Off Simulation and Thermal Decomposition of Confined High Energetic Material. *Propellants. Explos. Pyrotech.* **2015**, *40*(5): 699-705; https://doi.org/10.1002/prep.201400296.

[7] McCallen, R.; Dunn, T.; Nichols, A.; Reaugh, J.; McClelland, M. Modeling of Thermal Convection of Liquid TNT for Cook-off. *Proc. Nuclear Explosives Code Development Conf.*, Monterey, US-CA, **2002**.

[8] Hobbs, M.L.; Kaneshige, M.J.; Gilbert, D.W.; Marley, S.K.; Todd, S.N. Modeling TNT Ignition. *J. Phys. Chem. A*. **2009**, *113*(39): 10474-10487; https://doi.org/10.1021/jp906134f.

[9] Hobbs, M.L.; Kaneshige, M.J. The Effect of Venting on Cookoff of a Melt-castable Explosive (Comp-B). *Sci. Technol. Energ. Mater.* **2015**, *76*(3): 68-74.

[10] Sarangapani, R.; Ramavat, V.; Reddy, S.; Subramanian, P.; Sikder, A.K. Rheology Studies of NTO-TNT Based Melt-cast Dispersions and Influence of Particle-Dispersant Interactions. *Powder Technol.* **2015**, *273*: 118-124; https://doi.org/10.1016/j.powtec.2014.12.013.
[11] Zerkle, D.K.; Núñez, M.P.; Zucker, J.M. Molten Composition B Viscosity at Elevated Temperature. *J. Energ. Mater*. **2016**, *34*(4): 368-383; https://doi.org/10.1080/07370652.2015.1102179.
[12] Hobbs, M.L.; Kaneshige, M.J.; Erikson, W.W. Predicting Large-scale Effects During Cookoff of PBXs and Melt-castable Explosives. *Proc. 26th Int. Colloquium on the Dynamics of Explosions and Reactive Systems,* Boston, US-MA, **2017**.
[13] Davis, S.M.; Zerkle, D.K.; Smilowitz, L.B.; Henson, B.F.; Suvorova, N.A.; Remelius, D.K. Integrated Rheology Model: Explosive Composition B-3. *J. Energ. Mater*. **2018**, *36*(4): 398-411; https://doi.org/10.1080/07370652.2018.1451573.
[14] Davis, S.M.; Zerkle, D.K.; Smilowitz, L.B.; Henson, B.F. Molten Composition B-3 Yield Stress Model. *AIP Conf. Proc.* **2018**, *1979*: paper 150011; https://doi.org/10.1063/1.5044967.
[15] Davis, S.M.; Zerkle, D.K. Estimation of Yield Stress/Viscosity of Molten Octol. *AIP Adv.* **2018**, *8*: paper 055202; https://doi.org/10.1063/1.5027397.
[16] Du, L.-x.; Jin, S.-h.; Shu, Q.-h.; Li, L.-j.; Chen, K.; Chen, M.-l.; Wang, J.-f. The Investigation of NTO/HMX-based Plastic-bonded Explosives and Its Safety Performance. *Def. Technol.* **2021**, *18*(1): 72-80; https://doi.org/10.1016/j.dt.2021.04.002.
[17] Victor, A.C. Simple Calculation Methods for Munitions Cookoff Times and Temperatures. *Propellants. Explos. Pyrotech.* **1995**, *20*(5): 252-259; https://doi.org/10.1002/prep.19950200506.
[18] Ye, Q.; Yu, Y.-g. Numerical Analysis of Cook-off Behavior of Cluster Tubular Double-based Propellant. *Appl. Therm. Eng.* **2020**, *181*: paper 115972; https://doi.org/10.1016/j.applthermaleng.2020.115972.
[19] *Slow Heating, Munitions Test Procedures.* STANAG 4382 Ed. 2, **2003**.
[20] Zhi, X.-Q.; Hu, S.-Q.; Li, J.J.; Xu, S.-P.; Li, Y. RDX-based Booster Explosive Response Character Under Slow Cook-Off Conditions. *J. Energ. Mater*. **2011**, *29*(2): 75-87; https://doi.org/10.1080/07370650903535515.
[21] Zhu, M.; Wang, S.-a.; Huang, H.; Huang, G.; Wu, F.; Sun, S.-h.; Li, B.; Xu, Z.-j. Numerical and Experimental Study on the Response Characteristics of Warhead in the Fast Cook-off Process. *Def. Technol.* **2021**, *17*(4): 1444-1452; https://doi.org/10.1016/j.dt.2020.08.001.
[22] Rajagopal, T.K.R.; Ramachandran, R.; James, M.; Gatlewar, S.C. Numerical Investigation of Fluid Flow and Heat Transfer Characteristics on the Aerodynamics of Ventilated Disc Brake Rotor Using CFD. *Therm. Sci.* **2014**, *18*(2): 667-675; https://doi.org/10.2298/TSCI111219204R.
[23] Wen, Q.; Wang, Y.; Wang, G.; Chang, T.; Yan, L. Numerical Analysis of Response of a Fuze to Cook-off. *J. Energ. Mater*. **2019**, *37*(3): 340-355; https://doi.org/10.1080/07370652.2019.1615580.

[24] Hobbs, M.L.; Kaneshige, M.J.; Anderson, M.U. Cook-off of a Melt-castable Explosive (COMP-B). *Proc. 27th JANNAF Propulsion Systems Hazards Joint Subcommittee Meeting,* Monterrey, US- CA, **2012**.
[25] Moore, D.W.; Burkardt, L.A.; McEwan, W. Viscosity and Density of the Liquid System TNT-Picric Acid and Four Related Pure Materials. *J. Chem. Phys*. **1956**, *25*(6): 1235-1241; https://doi.org/10.1063/1.1743185.
[26] Parry, M.A.; Billon, H.H. Flow Behaviour of Molten 2,4,6-Trinitrotoluene (TNT) Between Concentric Cylinders. *Rheol. Acta* **1990**, *29*(5): 462-468; https://doi.org/10.1007/BF01376797.
[27] Parry, M.A.; Billon, H.H. A Note on the Coefficient of Viscosity of Pure Molten 2,4,6-Trinitrotoluene (TNT). *Rheol. Acta* **1988**, *27*: 661-663; https://doi.org/10.1007/BF01337463.
[28] Joshi, V.; Vadali, S.; Wasnik, R.; Jangid, S.; Maurya, M. Studies on Rheological Properties and Process Parameters of TNT based Castable High Explosive Compositions. *Sci. Technol. Energ. Mater.* **2017**, *78*(4): 87-92.
[29] Abdali, S.S.; Mitsoulis, E.; Markatos, N.C. Entry and Exit Flows of Bingham Fluids. *J. Rheol.* **1992**, *36*(2): 389-407; https://doi.org/10.1122/1.550350.
[30] Coussot, P. Slow Flows of Yield Stress Fluids: Yielding Liquids or Flowing Solids? *Rheol. Acta* **2018**, *57*(1): 1-14; https://doi.org/10.1007/s00397-017-1055-7.
[31] Jerkins, M.; Schröter, M.; Swinney, H.L.; Senden, T.J.; Saadatfar, M.; Aste, T. Onset of Mechanical Stability in Random Packings of Frictional Spheres. *Phys. Rev. Lett.* **2008**, *101*: paper 018301; https://doi.org/10.1103/PhysRevLett.101.018301.
[32] Liang, T.; Zhang, Y.; Ma, Z.; Guo, M.; Xiao, Z.; Zhang, J.; Dong, M.; Fan, J.; Guo, Z.; Liu, C. Energy Characteristics and Mechanical Properties of Cyclotrimethylenetrinitramine (RDX)-based Insensitive High-Energy Propellant. *J. Mater. Res. Technol.* **2020**, *9*(6): 15313-15323; https://doi.org/10.1016/j.jmrt.2020.09.132.
[33] Sanhye, W.; Dubois, C.; Laroche, I.; Pelletier, P. Numerical Modeling of the Cooling Cycle and Associated Thermal Stresses in a Melt Explosive Charge. *AIChE J.* **2016**, *62*(10): 3797-3811; https://doi.org/10.1002/aic.15288.
[34] Turner, R.H.; Cimbala, J.M.; Yunus, A.; Cengel, D. *Fundamentals of Thermal-Fluid Sciences*. 5th Ed., McGraw-Hill Education, New York, **2016**, pp. 829-830; ISBN 978-0-07-802768-0.

Received: September 28, 2021
Revised: September 29, 2023
First published online: September 29, 2023